# Three-Dimensional Fe Speciation of an Inclusion Cloud within an Ultradeep Diamond by Confocal μ-X-ray Absorption Near Edge Structure: Evidence for Late Stage Overprint

**8 AUTHORS**, INCLUDING:

**Geert Silversmit**
Belgian Cancer Registry
**90** PUBLICATIONS   **1,172** CITATIONS

SEE PROFILE

**Bart Vekemans**
Ghent University
**160** PUBLICATIONS   **2,316** CITATIONS

SEE PROFILE

**Karen Appel**
European XFEL
**182** PUBLICATIONS   **1,477** CITATIONS

SEE PROFILE

**Laszlo Vincze**
Ghent University
**221** PUBLICATIONS   **4,185** CITATIONS

SEE PROFILE

# Three-Dimensional Fe Speciation of an Inclusion Cloud within an Ultradeep Diamond by Confocal $\mu$-X-ray Absorption Near Edge Structure: Evidence for Late Stage Overprint

Geert Silversmit,*[†] Bart Vekemans,[†] Karen Appel,[‡] Sylvia Schmitz,[§] Tom Schoonjans,[†] Frank E Brenker,[§] Felix Kaminsky,[||] and Laszlo Vincze[†]

[†]X-ray Microspectroscopy and Imaging Research Group (XMI), Department of Analytical Chemistry, Ghent University, Krijgslaan 281 S12, B-9000 Gent, Belgium

[‡]HASYLAB at DESY, Notkestrasse 85, D-22607 Hamburg, Germany

[§]Geoscience Institute-Mineralogy, Goethe University, Altenhoeferallee 1, 60438 Frankfurt am Main, Germany

[||]KM Diamond Exploration Ltd., 2446 Shadbolt Lane, West Vancouver, BC, Canada, V7S 3J1

**ABSTRACT:** A stream of $1-20$ $\mu$m sized mineral inclusions having the negative crystal shape of its host within an "ultra-deep" diamond from Rio Soriso (Juina area, Mato Grosso State, Brazil) has been studied with confocal $\mu$-X-ray absorption near edge structure ($\mu$XANES) at the Fe K and Mn K edges. This technique allows the three-dimensional nondestructive speciation of the Fe and Mn containing minerals within the inclusion cloud. The observed Fe-rich inclusions were identified to be ferropericlase (Fe,Mg)O, hematite and a mixture of these two minerals. Confocal $\mu$-X-ray fluorescence ($\mu$XRF) further showed that Ca-rich inclusions were present as well, which are spatially separated from or in close contact with the Fe-rich inclusions. The inclusions are aligned along a plane, which most likely represents a primary growth zone. In the close vicinity of the inclusions, carbon coated planar features are visible. The three-dimensional distribution indicates a likely fluid overprint along an open crack. Our results imply that an imposed negative diamond shape of an inclusion alone does not exclude epigenetic formation or intense late stage overprint.
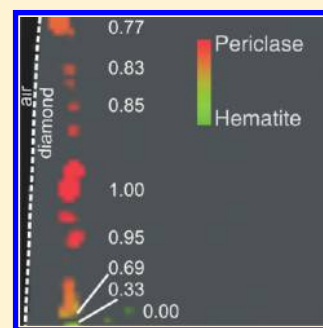


Until recently, only indirect methods based on high-pressure techniques and seismological data were applied to study the composition and conditions of the deep Earth.[1,2] During the last decade, inclusions in "ultra-deep" natural diamond crystals provided a unique possibility to study the Earth's mantle to depths reaching even the lower mantle (>670 km).[3−8] During the growth of a natural diamond, fluids, minerals, and rock fragments can be trapped inside it. These inclusions are then shielded from the environment during the transport of the diamond toward the Earth's surface, preserving their original capture composition and, in some cases, even their high pressure structure.[3−9] In this way, these inclusions provide the most direct way to derive information on the composition and structure of the deep Earth.[3−9]

The majority of natural diamond crystals are formed in the Earth's lithospheric upper mantle ($\sim$100−200 km depth).[10] Only a few sources, e.g., Juina (Brazil) and Kankan (Guinea), provide rare so-called "ultra-deep" diamond crystals which were formed in the astenospheric upper mantle, the transition zone (410−670 km), and even the lower mantle (>670 km) of the Earth.[4,7,9] These unique diamond crystals and their inclusions are the only direct source of information available on the chemical and structural conditions in the deep Earth down to the lower mantle.[3−9,11−15] The main uncertainty in the study of these inclusions is to distinguish between pre- and syngenetic mineral inclusions and a possible epigenetic formation or overprint.[16] In order to preserve the enclosed nature of the inclusions, a nondestructive

in situ analysis method is desired. In this respect, X-ray techniques like $\mu$-X-ray fluorescence ($\mu$XRF), $\mu$-X-ray diffraction ($\mu$XRD), and $\mu$-X-ray absorption spectroscopy ($\mu$XAS) can be very useful. However, because of the high X-ray scattering power of the diamond host, a confocal detection mode is needed in order to examine the mostly complex, polyphase inclusions inside the diamond. The feasibility of confocal $\mu$-X-ray absorption near edge structure ($\mu$XANES) has been demonstrated recently.[17,18]

## ■ MATERIALS AND METHODS

The confocal $\mu$XANES and $\mu$XRF experiments were performed at the scanning XRF microprobe installed at Beamline L of the 4.44 GeV positron storage ring DORIS III at HASYLAB (Hamburg, Germany). This bending magnet station (magnetic field strength of 1.2 T, critical energy of 16.04 keV) is dedicated to scanning (confocal) $\mu$XRF and $\mu$XANES and is equipped with a Si(111) double crystal monochromator (energy resolution $\Delta E/E \sim 10^{-4}$) for XAS measurements. The X-ray beam is focused by a large acceptance glass polycapillary lens having a focal distance of 4.8 mm (XOS Inc., Albany). The photon flux in the focused beam was approximately $10^9-10^{10}$ photons/s. The incoming and transmitted X-ray beam intensities are monitored

by 100 and 280 mm long ionization chambers, respectively. The X-ray fluorescence radiation is detected by a Vortex-EX silicon drift detector (SII NanoTechnology USA Inc., having a detector area of 50 mm$^2$, 350 $\mu$m crystal thickness, measured energy resolution of 180 eV at Fe—K$\alpha$) placed under 90° with respect to the incoming X-ray beam in the horizontal (storage ring) plane. The confocal detection was realized by mounting a second polycapillary half-lens (XOS Inc., focal distance 2.1 mm) in front of the energy dispersive detector. A photograph of the employed confocal sample setup can be found in ref 19.

The excitation energy for the confocal $\mu$XRF experiments was fixed at 7200 eV using the double crystal Si(111) monochromator. For the $\mu$XRF imaging, the measured intensities were normalized to a constant synchrotron beam current of 100 mA using the count rate from the first ionization chamber. The raw XRF spectra were converted into elemental net peak intensities using the nonlinear least-squares fitting software package AXIL/MICROXRF2. This software package is dedicated to the accurate deconvolution of large numbers of energy-dispersive XRF spectra collected during micro-XRF scans, including background subtraction and the elimination of peak overlap and other spectral artifacts, such as detector escape and sum peaks.[20]

The energy scale for the XANES measurements was calibrated by setting the first inflection point in the Fe K XANES transmission spectrum of a 5 $\mu$m thick Fe foil to 7112 eV. Fe K and Mn K XANES spectra were collected from about 100 eV before the absorption edge up to 150 eV beyond the edge, with an energy step of 0.5 eV in the edge region. The measurement time per energy step for the Fe K XANES spectra was 2 s in the pre-edge region (7000−7100 eV) and 5 s in the edge and postedge region (7100−7250), for the Mn K XANES spectra this was 2 s in the pre-edge region (6460−6540 eV) and 8 s in edge and postedge region (6540−6660 eV). Typically 2−6 spectra were averaged for the Fe K XANES and 10−19 spectra for the Mn K XANES. The double crystal monochromator was detuned to 70% for the higher harmonics rejection. The XANES linear combination method used is described previously.[21] The algorithm takes into account the standard deviation on the XANES data, determined from multiple scans.

Line scans of a 10 $\mu$m thick stainless steel wire (AISI302, Fe/Cr18/Ni8, Goodfellow) in the focal plane of the focusing polycapillary were performed to determine the full-width-at-half-maxima (fwhm) of the confocal ellipsoidal detection volume for an incoming X-ray beam with an energy of 7200 eV. The intensity profiles of the transmitted signal from a horizontal and vertical wire scan were used to determine the horizontal and vertical beam sizes. Deconvoluting these intensity profiles taking into account the wire thickness and its cylindrical shape gives Gaussian profiles of which the fwhm are taken as a measure for the horizontal and vertical beam sizes, $D_{b,h}$ and $D_{b,v}$. A similar procedure on the Fe K$\alpha$ fluorescence intensity profile for the vertical wire scan gives the vertical fwhm, $S_V$, of the confocal detection volume. Together with the vertical beam size, the confocal acceptance, $S_A$, for Fe K$\alpha$ can be calculated from $(1/S_V)^2 = (1/S_A)^2 + (1/D_{b,v})^2$.[17,22] The horizontal beam-size, $D_{b,h}$, and the confocal polycapillary acceptance, $S_A$, together determine the fwhm of the detection volume in the horizontal plane.[17,22]

Elemental detection limits were determined using a 1 mm thick NIST SRM611 standard (trace elements in glass). A depth scan along the sample normal was performed first to determine the optimal measuring location. A maximum count rate was
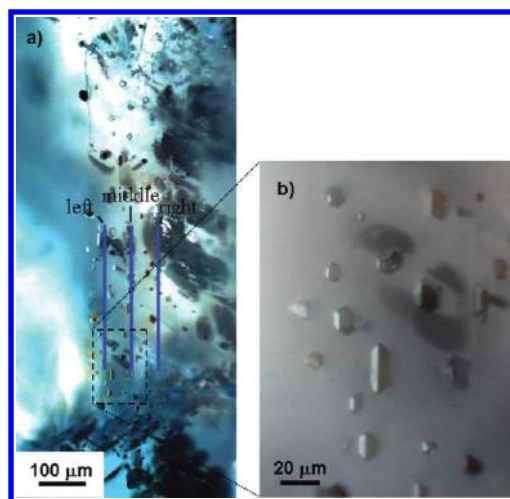


**Figure 1.** (a) Optical image of a part of the swarm of inclusions in diamond RS69. The approximate positions of the vertical confocal $\mu$XRF maps recorded are indicated by the blue lines; (b) zoom on the indicated area showing cuboctahedra, rhombododecahedral, and distorted octahedral shapes of the inclusions, indicative of their syngenetic formation.

obtained at a depth of about 15 $\mu$m, and a confocal $\mu$XRF spectrum with a measuring time of 1000 s was recorded at that depth with an excitation energy of 7.2 keV. The elemental detection limit calculation was based on the confocal model of Malzer and Kanngiesser.[22]

The examined diamond (RS69) was collected from an alluvial deposit in the Juina area (Mato Grosso State, Brazil), a well-known source of ultradeep diamond crystals.[6,7] This diamond contains a stream of micrometer-sized inclusions, as shown in Figure 1. The inclusions show cuboctahedral, rhombododecahedral, and distorted octahedral shapes representing the negative crystal shape of the diamond (see Figure 1), which indicates the syngenetic formation of the inclusion and the diamond host.

However, all inclusions are aligned along a flat plane, which could be a growth zone or healed crack. In contrast, the overprint clearly follows a crack penetrating through at least part of the diamond host. In order to access the inclusions within the diamond with the confocal setup and to reduce matrix absorption, a window was polished in the diamond very close to the inclusion stream (on the order of 100 $\mu$m or less). The diamond was subsequently mounted with the polished surface vertically and placed at an angle of 45° with respect to the incoming $\mu$beam and the detector axis. A horizontal confocal $\mu$XRF plane was measured first to locate the inclusion stream. Then, three vertical confocal $\mu$XRF planes perpendicular to the polished diamond surface and separated by 50 $\mu$m distance were recorded using a measuring time of 5 s per voxel. The approximate locations of these maps are indicated in Figure 1.

## ■ RESULTS

**Characterization of the Confocal $\mu$beam Setup.** *Confocal Detection Volume.* The vertical and horizontal beam sizes (fwhm), $D_{b,v}$ and $D_{b,h}$, were measured to be 22.7 and 20.7 $\mu$m. The vertical fwhm of the ellipsoidal detection volume was 17.0 $\mu$m, which gives an acceptance, $S_A$, of 25.6 $\mu$m for Fe K$\alpha$. As a result, the dimensions (fwhm) for the ellipsoidal confocal

detection volume at the Fe K edge were determined to be 21 × 26 × 17 $\mu m^3$ ($D_{b,h} \times S_A \times S_V$).

*Elemental Detection Limits.* The elemental detection limits for the confocal $\mu$-XRF setup for an excitation energy of 7200 eV and a measuring time of 1000 s are given in Figure 2. For the 3d transition metals probed (Ti—Fe), relative detection limits between 2 and 20 $\mu g/g$ are obtained. The extrapolated detection limits for a measurement time of 5 s/scan point, as used for collecting the elemental maps, are represented by the dashed curve. For Fe, a relative detection limit of approximately 30 $\mu g/g$ is achieved in the scanning mode for the confocal elemental maps. Elements lighter than Si are barely detected due to absorption by the air path to the detector and the detector window and dead layer.
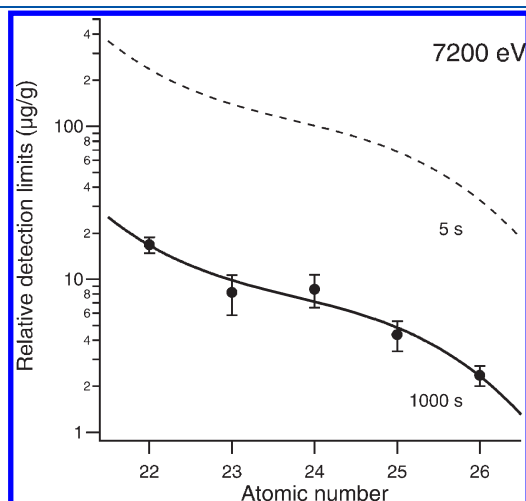


**Figure 2.** Relative elemental detection limits for the confocal $\mu$XRF measurements determined using a 1 mm thick NIST SRM611 standard for an incoming X-ray energy of 7200 eV and a measuring time of 1000 s (the error bars represent ±1 SD). The extrapolated values for a measuring time of 5 s are represented by the dashed curve.

**Elemental Imaging.** The elemental distributions for Ca, Cr, Mn, Fe and the intensity map of the scatter peak (composed of the sum of the integrated Compton and Rayleigh scatter peaks and the overlapping Fe K$\beta$ fluorescence line when an iron inclusion is detected) measured in the central map (see Figure 1) are given in Figure 3, together with the sum spectrum obtained by summing all individual voxel spectra from the scan. This sum spectrum shows the presence of Ca, Cr, Mn, and Fe. Although a weak K signal can be observed in the sum spectrum, the K intensity is below the detection limit attainable in the individual point spectra of the scan and will therefore not be considered further. The diamond surface can be observed in the intensity map of the scatter peak. This map further shows that the detected inclusions are at a depth between 30 and 60 $\mu m$ from the diamond surface, besides two deeper inclusions at the bottom of the map. The intensity of the scatter peak decreases at larger depths, due to self-absorption by the diamond matrix. There is a strong spatial correlation between Cr, Mn, and Fe, while the Ca appears at different locations.

An RGB overlay image of the above Ca, Mn, and Fe elemental maps is given in Figure 4 (middle), with the diamond host matrix represented by the dark gray area as derived from the scatter peak intensity map. This combined view forms an excellent visual representation of the complete confocal $\mu$XRF results. Similar combined RGB views for the two other vertical maps are also given in Figure 4. From these maps we can conclude that Fe and Mn are present in the same inclusions. The Ca rich inclusions are separated or in close contact with the Fe rich phases; however, they do not coincide, as can be seen in the left and middle maps of Figure 4. The Ca is therefore associated with inclusions having different (non Fe-rich) compositions.

**Mineral Identification by Confocal $\mu$XANES.** On a selection of the observed Fe-rich inclusions, confocal Fe K XANES spectra were recorded with a total number of 17 locations distributed over the three vertical maps. As a representative example, the Fe K XANES spectra for eight locations in the "left" confocal map are given in Figure 5 together with hematite ($Fe_2O_3$) and
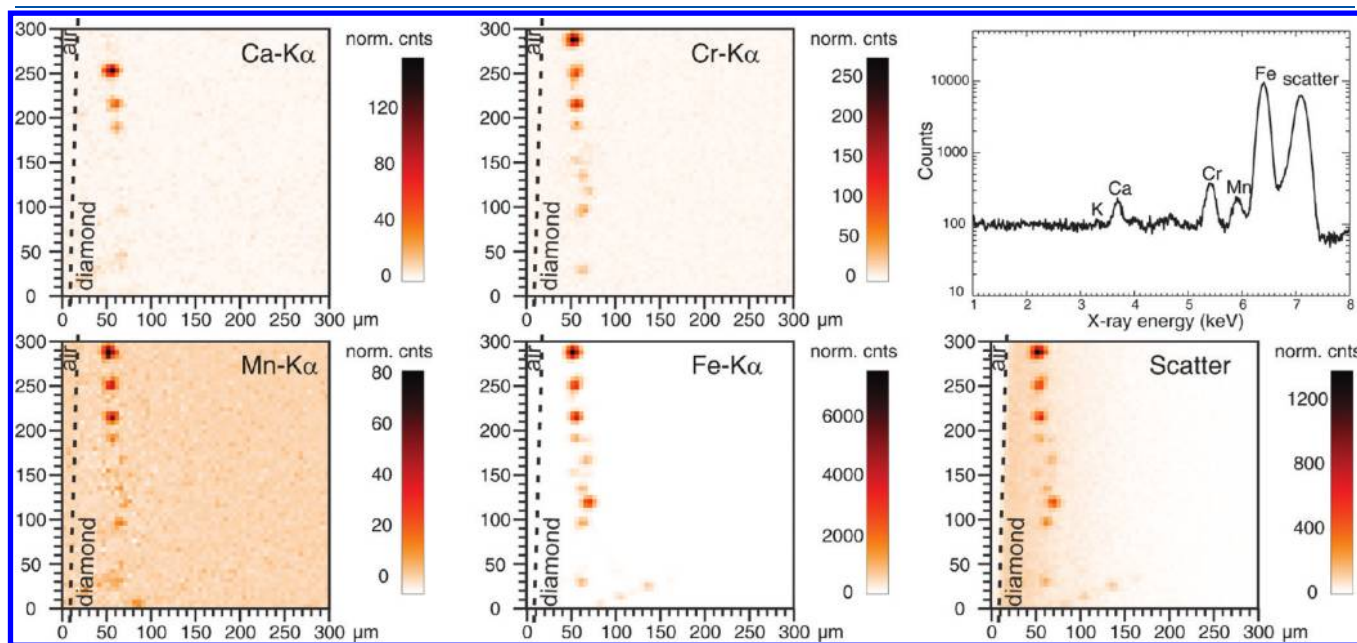


**Figure 3.** 2D distributions of calcium, chromium, manganese, and iron and the scatter peak for the central vertical confocal $\mu$XRF map within the RS69 diamond (61 × 5 $\mu m$ by 61 × 5 $\mu m$, 5 s). The sum spectrum is given in the top right.
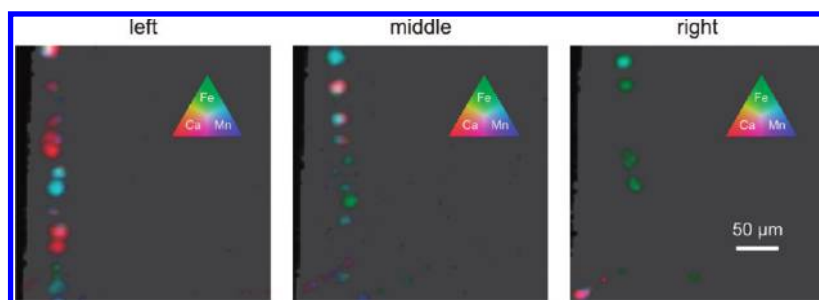
**Figure 4.** Combined RGB images showing the elemental distributions of Ca (red), Fe (green), and Mn (blue) for the three vertical confocal maps performed within diamond RS69 as indicated in Figure 1. The diamond matrix (detected based on the scatter peak) is shown in dark gray, which allows visualization of the diamond surface at the left of each map, and the part of the map that lies outside the diamond is given in black.
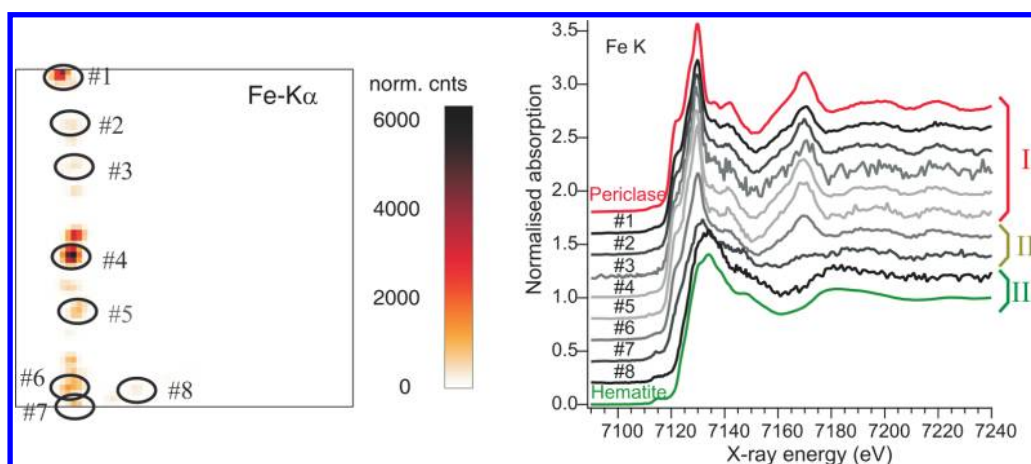


**Figure 5.** (left) Fe elemental map for the "left" vertical confocal plane within diamond RS69; (right) corresponding confocal Fe $K$ $\mu$XANES spectra for the indicated Fe hotspots, with a vertical offset for clarity.
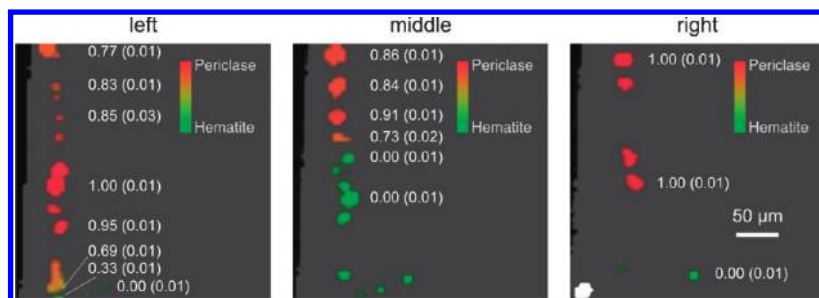


**Figure 6.** Combined RGB images showing the fraction of ferropericlase (red) and hematite (green) for the Fe-containing inclusions detected in the three vertical confocal maps performed within diamond RS69. The numbers give the fitted periclase fraction for the inclusions for which a Fe K XANES spectrum was measured. The diamond matrix is shown in dark gray, which allows visualization of the diamond surface at the left, and the part of the map that lies outside the diamond is given in black. The structure of the white inclusion remains unidentified.

ferropericlase ((Fe,Mg)O) reference spectra. The measurement locations are indicated on the corresponding Fe elemental map. The confocal ferropericlase Fe K XANES reference spectrum was obtained on an inclusion polished up to the surface of a similar diamond from the Mato Grosso state (Brazil) and identified by electron microprobe measurements. The measured confocal $\mu$XANES spectra of inclusions no. 1−5 are very similar to that obtained from ferropericlase, while inclusion no. 8 produces a XANES signature of hematite. As noted in Elemental Detection Limits, the Mg of the periclase compound cannot be observed in the confocal $\mu$XRF

spectra. Inclusions no. 6 and no. 7 have an intermediate Fe K XANES spectra. All measured Fe K XANES spectra could be analyzed as a linear combination of the periclase and hematite reference spectra. Figure 6 shows the corresponding periclase and hematite fit fractions for the detected Fe inclusions in the three confocal vertical maps in red and green, respectively. Pure ferropericlase was found in the upper half of the right map and for the two inclusions of the left map central in the inclusion stream. Pure hematite was found in the lower part of all maps. The other inclusions are mixtures with roughly 70−90% ferropericlase.
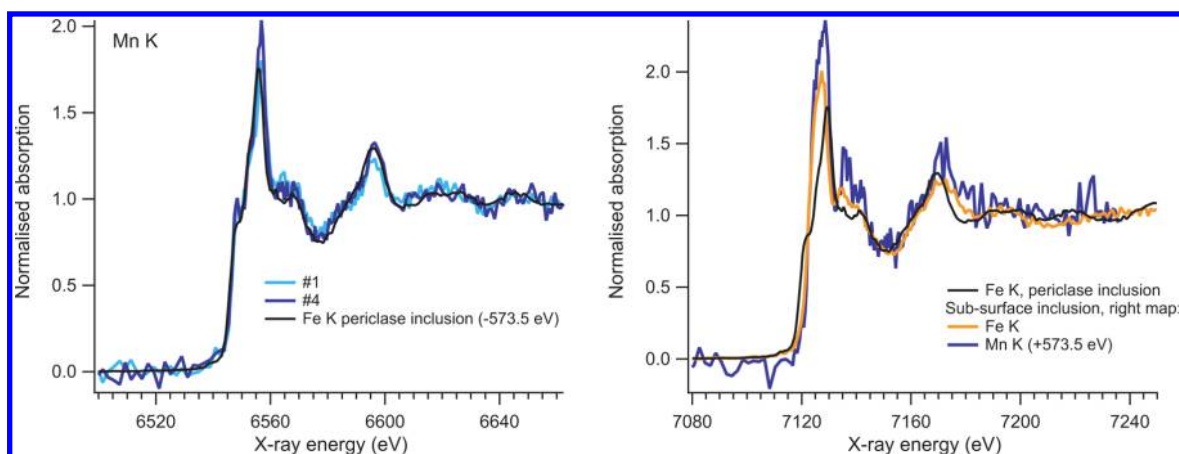
**Figure 7.** (left) Confocal Mn K $\mu$-XANES spectra for the inclusions no. 1 and no. 4 from Figure 5; (right) Fe K and shifted Mn K confocal XANES spectra for the near surface inclusion in the right confocal map.
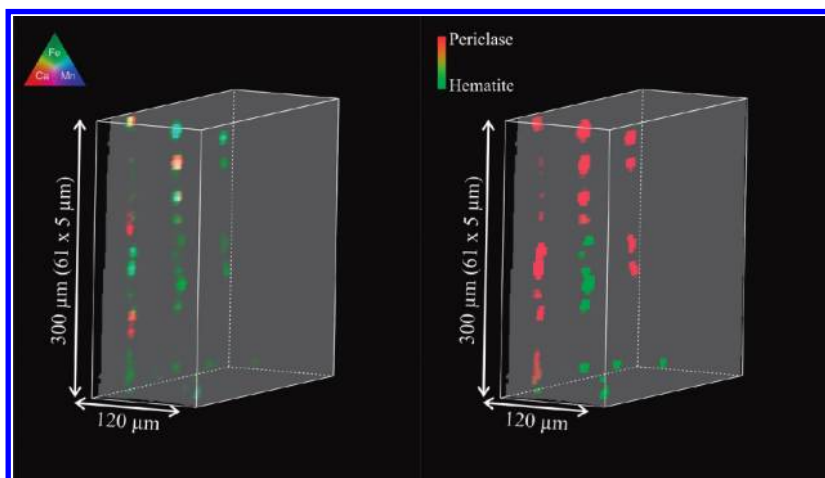


**Figure 8.** (left) Combined 3D RGB image showing the elemental distributions of Ca (red), Fe (green), and Mn (blue) for a 300 $\mu$m long part of the inclusion stream within diamond RS6; (right) interpolated composition image showing the fraction of periclase (red) and hematite (green) for the Fe containing inclusions. The diamond matrix is shown in dark gray.

The maps in Figure 6 were obtained as follows. A threshold was applied to the Fe K$\alpha$ fluorescence intensities within each vertical confocal map, in order to delineate each Fe containing inclusion. The periclase fraction of inclusions for which an Fe K XANES spectrum was measured is set to the value resulting from the linear combination fit. The periclase fraction for an inclusion for which no XANES spectrum was available was estimated from a linear interpolation using the fit fractions of the nearest measured inclusions above and below it. The composition of the inclusions in the lower part of the middle map was set to 100% hematite by extrapolation. Since both left and right maps have hematite in their lower part, this extrapolation is considered to be realistic.

Although the Mn fluorescence intensities are about 100 times smaller than the Fe fluorescence signal (see Figure 3), confocal XANES spectra were recorded for the most intense Mn spots present in the "left" and "right" confocal maps. The Mn K confocal XANES spectra for the inclusions identified as no. 1 and no. 4 in Figure 5 are given in Figure 7 (left). The Mn K XANES spectra for these inclusions have the same features as the corresponding Fe K XANES spectra given in Figure 5; the Mn atoms therefore occupy Fe sites within the mineral inclusion

crystal structure. The same conclusion could be drawn for the Mn K XANES spectrum collected for the top periclase inclusion of the right map (spectra not shown).

The lowest inclusion in the right map close to the diamond surface has Fe K and Mn K XANES spectra that are different from both hematite and periclase, see Figure 7 (right). Compared to the ferropericlase spectrum, the shoulder on the low energy side of the absorption edge is not present making the main edge start at a higher X-ray energy, the white line peak lies at a 2 eV lower position, while the postedge structure is comparable. The composition of this inclusion remains unidentified. As for the other inclusions, the Fe K and Mn K spectra are again very similar, showing that both metals occupy identical sites within the mineral crystal structure. The composition for this unidentified inclusion was not used for the phase identification given in Figure 6 and is represented by the white area.

## ◼ CONCLUSIONS

This work demonstrates a novel combined use of trace-level confocal $\mu$XANES and $\mu$XRF for the nondestructive, in situ

chemical characterization of microscopic inclusions in a unique natural "ultra-deep" diamond crystal together with a detailed analytical characterization of the experimental method. The elemental distributions of Ca, Cr, Mn, and Fe within a stream of 1−20 $\mu$m sized mineral inclusions within an ultradeep diamond from the Juina region in Brazil were determined with confocal $\mu$XRF. Fe, Cr, and Mn are jointly present, while the Ca rich inclusions represent different mineral phases which are spatially separated from but often in close contact with the Fe rich inclusions. A summary 3D view of the elemental distributions is given in Figure 8 (left). The Fe rich inclusions were determined to be composed of hematite, ferropericlase, and a mixture of these minerals. Confocal $\mu$XANES further showed that Mn, which is about 100 times less abundant than Fe, occupies Fe sites within the mineral crystal structure. A compilation of the determined Fe composition is shown in Figure 8 (right) demonstrating truly 3D resolved Fe speciation within a 300 $\mu$m long part of the inclusion stream.

Although the imposition of the dominant crystallographic faces of the diamond on the inclusion suite (Figure 1) would support a syngenetic or protogenetic origin of all inclusions,[23,24] the observed systematic occurrence suggests an epigenetic replacement from ferropericlase to the more oxidized hematite. Epigenetic alteration products in diamond are typically found along cracks and do not show a cuboctahedral shape.[25] Minerals crystallizing from a melt would evolve their own unique crystal habit in accordance to their crystal structure. Episodic growth of diamond is a well-known phenomenon.[26] However, it is unlikely in the present case as the replacement crosscut the pre-existing alignment of the inclusions rather than representing a core and rim structure. In the past, cuboctahedral shaped inclusions recovered from broken diamonds were treated as syngenetic in nature. Our new in situ 3D-XANES data show that a significant overprint of inclusions along pre-existing planar features is possible without changing their outer shape.

## ■ AUTHOR INFORMATION

### Corresponding Author
*E-mail: Geert.Silversmit@UGent.be. Fax: + 32 9 264 4960.

## ■ ACKNOWLEDGMENT

## ■ REFERENCES

(1) Duffy, T. S. Rep. Prog. Phys. 2005, 68, 1811–1859.

(2) Romanowicz, B. Annu. Rev. Earth Planet. Sci. 2003, 31, 303–328.

(3) Harte, B.; Harris, J. W.; Hutchison, M. T.; Watt, G. R.; Wilding, M. C. In Mantle Petrology: Field Observations and High Pressure Experimentation: A Tribute to Francis R. (Joe) Boyd; Fei, Y., Bertka, C. M., Mysen, B. O., Eds.; Geochemical Society: Houston, TX, 1999; Vol. 6, pp 125−153.

(4) Stachel, T.; Harris, J. W.; Brey, G. P.; Joswig, W. Contrib. Mineral. Petrol. 2000, 140, 16–27.

(5) Stachel, T. Eur. J. Mineral. 2001, 13, 883–892.

(6) Kaminsky, F.; Zakharchenko, O. D.; Davies, R.; Griffin, W. L.; Khachatryan-Blinova, G. K.; Shiryaev, A. Contrib. Mineral. Petrol. 2001, 140, 734–753.

(7) Hayman, P.; Kopylova, M.; Kaminsky, F. Contrib. Mineral. Petrol. F 2005, 149, 430–445.

(8) Tappert, R.; Stachel, T.; Harris, J. W.; Muehlenbachs, K.; Ludwig, T.; Brey, G. P. Geology 2005, 33, 565–568.

(9) Brenker, F. E.; Stachel, T.; Harris, J. W. Earth Planet. Sci. Lett. 2002, 198, 1–9.

(10) Boyd, F. R.; Gurney, J. J.; Richardson, S. H. Nature 1985, 315, 387–389.

(11) Vincze, L.; Vekemans, B.; Brenker, F. E.; Falkenberg, G.; Rickers, K.; Somogyi, A.; Kersten, M.; Adams, F. Anal. Chem. 2004, 76, 6786–6791.

(12) Stachel, T.; Brey, G. P.; Harris, J. W. Contrib. Mineral. Petrol. 2000, 140, 1–15.

(13) Tappert, R.; Stachel, T.; Harris, J. W.; Muehlenbachs, K.; Ludwig, T.; Brey, G. P. Geology 2005, 33, 565–568.

(14) Wirth, R.; Vollmer, C.; Brenker, F. E.; Matsyuk, S.; Kaminsky, F. Earth Planet. Sci. Lett. 2007, 259, 384–399.

(15) Brenker, F. E.; Vincze, L.; Vekemans, B.; Nasdala, L.; Stachel, T.; Vollmer, C.; Kersten, M.; Somogyi, A.; Adams, F.; Joswig, W.; Harris, J. W. Earth Planet. Sci. Lett. 2005, 236, 579–587.

(16) Taylor, L. A.; Anand, M.; Promprated, P.; Taylor, L. A.; Anand, M.; Promprated, P. In 8th International Kimberlite Conference, Victoria, Canada, 2003; extended abstract.

(17) Silversmit, G.; Vekemans, B.; Nikitenko, S.; Schmitz, S.; Schoonjans, T.; Brenker, F. E.; Vincze, L. Phys. Chem. Chem. Phys. 2010, 12, 5653–5659.

(18) Silversmit, G.; Vekemans, B.; Nikitenko, S.; Bras, W.; Brenker F. E.; Vincze, L. J. Phys.: Conf. Ser. 2009, 190

(19) De Samber, B.; Silversmit, G.; De Schamphelaere, K.; Evens, R.; Schoonjans, T.; Vekemans, B.; Janssen, C.; Masschaele, B.; Van Hoorebeke, L.; Szaloki, I.; Vanhaecke, F.; Rickers, K.; Falkenberg, G.; Vincze, L. J. Anal. At. Spectrom. 2010, 25, 544–553.

(20) Vekemans, B.; Janssens, K.; Vincze, L.; Adams, F.; Van Espen, P. X-ray Spectrom. 1994, 23, 278–285.

(21) Tirez, K.; Silversmit, G.; Vincze, L.; Servaes, K.; Vanhoof, C.; Mertens, M.; Bleux, N.; Berghmans, P. J. Anal. At. Spectrom. 2011, 26, 517–527.

(22) Malzer, W.; Kanngiesser, B. Spectrochim. Acta, Part B: At. Spectrosc. 2005, 60, 1334–1341.

(23) Harris, J. W. In The Properties of Diamond; Field, J. E., Ed.; Academic Press: London, 1979; pp 555−591.

(24) Brenker, F. E.; Vollmer, C.; Vincze, L.; Vekemans, B.; Szymanski, A.; Janssens, K.; Szaloki, I.; Nasdala, L.; Joswig, W.; Kaminsky, F. Earth Planet. Sci. Lett. 2007, 260, 1–9.

(25) Harris, J. W. Ind. Diamond Rev. 1968, 28 (Part I, 402−410 and Part II), 458−461.

(26) Richardson, S. H.; Shirey, S. B.; Harris, J. W. Lithos 2004, 77, 143–154.